Int. J. Heat Mass Transfer. Vol. 27, No. 5, pp. 755–772, 1984
Printed in Great Britain

0017-9310/84 $3.00 + 0.00

LAMINAR AND TURBULENT NATURAL CONVECTION IN AN ENCLOSED CAVITY

N. C. MARKATOS* and K. A. PERICLEOUS

Concentration Heat and Momentum Limited, 40 High Street, Wimbledon, London SW19 5AU, U.K.

(*Received* 9 *May* 1983 *and in revised form* 3 *October* 1983)

Abstract—The paper presents a computational method used to obtain solutions of the buoyancy-driven laminar and turbulent flow and heat transfer in a square cavity with differentially heated side walls. A series of Rayleigh numbers, ranging from 10^3 to 10^{16} was studied. Donor-cell differencing is used, and mesh-refinement studies have been performed for all Rayleigh numbers considered. The turbulence model used for Rayleigh numbers greater than 10^6 is a ($k \sim \varepsilon$) two-equation model of turbulence, that includes gravity $\sim$ density gradient interactions. The results are presented in tabular and graphical form, and as correlations of the Nusselt and Rayleigh numbers. Furthermore, the results for Rayleigh numbers up to 10^6 are compared with the benchmark numerical solution of de Vahl Davis.

NOMENCLATURE

D	cavity width [m]
g	gravitational acceleration [m s^{-2}]
k	kinetic energy of turbulence per unit mass [J kg^{-1}]
Nu	Nusselt number
Pr	Prandtl number
Ra	Rayleigh number, $\rho^2 g D^3 \beta \Delta T\ Pr/\mu^2$
S	source term
T	temperature [K]
v	velocity component in the y-direction [m s^{-1}]
w	velocity component in the z-direction [m s^{-1}]
y, z	spatial coordinates [m]
$\bar{y}, \bar{z}$	normalized coordinates.

1. INTRODUCTION

THE DETERMINATION of buoyancy-driven flow in an enclosed cavity provides a suitable comparison problem for evaluating the performance of numerical methods dealing with viscous flow calculations [1–3]. Furthermore, the above process has many practical applications of which the most widely known is that of double glazing. Other applications include nuclear-reactor insulation, ventilation of rooms, solar-energy collection and crystal growth in liquids. There is an ever increasing amount of research on confined natural convection and refs. [4–10] are typical examples of such work. A recent review of the existing literature is given by Ostrach [11]. Despite all the recent research activity, a central problem that has remained unsolved is the coupling between boundary layers and core flows. The latter depend on the boundary layer, which, in turn, is influenced by the core. This problem was first identified by Ostrach [5] and discussed more fully in refs. [6, 7]. The purpose of this work is to describe a computational procedure for solving the non-linear, coupled differential elliptic equations over the entire flow domain, with no assumptions concerning the core configuration or any other *ad hoc* simplification for Rayleigh numbers up to 10^6, and with the speculative use of a two-equation turbulence model for higher Rayleigh numbers; and to demonstrate that this can be accomplished without excessive demands on computer time or storage. The presented results are restricted to rectangular cavities of aspect ratio 1, fluids of Prandtl number 0.71, and Rayleigh numbers ranging from 10^3 to 10^{16}. However, the procedure is general and can be easily applied for practical computations in cavities of different aspect ratios, fluids of different Prandtl numbers, three-dimensional (3-D) enclosures or tilted enclosures such as, for example, those studied by Catton [4].

2. THE PROBLEM CONSIDERED

The problem considered is depicted schematically in Fig. 1, and refers to the two-dimensional (2-D) flow in a square cavity, of side D. The cavity is assumed to be of infinite depth along the x-axis and is heated differentially along the South (low-y) and North (high-y) walls. The other two (horizontal) walls are insulated.

The no-slip condition is applied on the velocity at all four walls, and friction is calculated by invoking 'wall-functions' [12], see Appendix. The hot and cold walls are considered to be isothermal, and the other two adiabatic. Heat transfer through the walls causes density changes to the fluid in the cavity, and leads to buoyancy-driven recirculation. The resulting flow is treated as steady and, depending on the Rayleigh number, laminar ($Ra \leqslant 10^6$) or turbulent ($Ra > 10^6$). This criterion for switching over to turbulence calculations is based on experimental observations [25, 26] and has been used widely in the literature [1–3, 20,

---

* Present address: Faculty of Science and Mathematics, School of Mathematics, Statistics and Computing, Thames Polytechnic, London SE18 6PF, U.K.

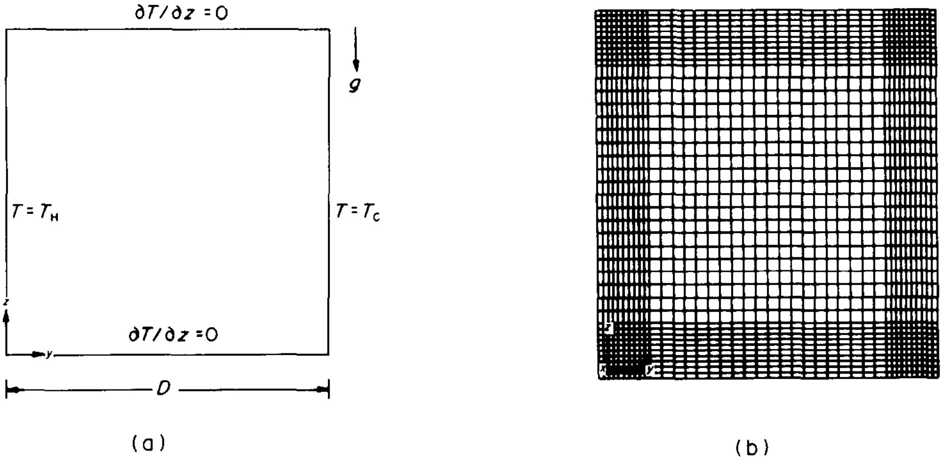

FIG. 1. (a) The process considered. (b) The solution grid used for $Ra \leqslant 10^6$.

22]. Reference fluid properties were calculated at the ambient temperature $T_0 = 293$ K.

3. MATHEMATICAL FORMULATION AND METHOD OF SOLUTION

3.1. *The differential equations*

For steady flow, the equations for continuity, velocity components and temperature take the form: continuity

$$\frac{\partial(\rho v)}{\partial y} + \frac{\partial(\rho w)}{\partial z} = 0; \tag{1}$$

y-direction momentum

$$\frac{\partial}{\partial z}(\rho v w) + \frac{\partial}{\partial y}(\rho v v) = \frac{\partial}{\partial z}\left(\mu \frac{\partial v}{\partial z}\right) + \frac{\partial}{\partial y}\left(\mu \frac{\partial v}{\partial y}\right) + S_v; \tag{2}$$

z-direction momentum

$$\frac{\partial}{\partial z}(\rho w w) + \frac{\partial}{\partial y}(\rho v w) = \frac{\partial}{\partial z}\left(\mu \frac{\partial w}{\partial z}\right) + \frac{\partial}{\partial y}\left(\mu \frac{\partial w}{\partial y}\right) + S_w; \tag{3}$$

general transported fluid scalar, ϕ (e.g. T, k, ε)

$$\frac{\partial}{\partial z}(\rho w \phi) + \frac{\partial}{\partial y}(\rho v \phi) = \frac{\partial}{\partial z}\left(\Gamma_\phi \frac{\partial \phi}{\partial z}\right) + \frac{\partial}{\partial y}\left(\Gamma_\phi \frac{\partial \phi}{\partial y}\right) + S_\phi; \tag{4}$$

where Γ_ϕ is the exchange coefficient for the transport of property ϕ. The source terms in the momentum equations are

$$S_w = \frac{\partial}{\partial x}\left(\mu \frac{\partial w}{\partial x}\right) + \frac{\partial}{\partial y}\left(\mu \frac{\partial v}{\partial z}\right) - \frac{\partial p}{\partial z} + \rho g \frac{\theta}{T_0}; \tag{5}$$

$$S_v = \frac{\partial}{\partial z}\left(\mu \frac{\partial w}{\partial y}\right) + \frac{\partial}{\partial y}\left(\mu \frac{\partial v}{\partial y}\right) - \frac{\partial p}{\partial y}; \tag{6}$$

$$S_T = 0,$$

where θ is the temperature rise above ambient T_0.

For Rayleigh numbers above 10^6 a two-equation ($k \sim \varepsilon$) turbulence model was used. Then the above equations are time-averaged equations and μ and Γ_ϕ are replaced by their 'effective' values μ_{eff} and Γ_{eff}, as given by the turbulence model [12, 13].

The generation term in the k-equation includes the buoyancy production

$$G_B = -\beta g \frac{\mu_t}{\sigma_{t,\phi}} \frac{\partial \phi}{\partial y}. \tag{7}$$

In stable stratification, G_B becomes a sink term so that the turbulent mixing is reduced. In unstable stratification, the buoyancy will enhance turbulence since G_B is positive. The buoyancy term appearing tentatively in the ε-equation, in other $k \sim \varepsilon$ calculations for buoyant flows [14, 24], has been omitted. There is no obvious physical reason for including such a term and other related work indicated that it is completely insignificant [15]. The turbulence model contains five constants which were assigned the following values [12]

$$C_1 = 1.44; \quad C_2 = 1.92; \quad C_\mu = 0.09;$$

$$\sigma_k = 1.0; \quad \sigma_\varepsilon = 1.314.$$

More details may be found in refs. [14, 15].

Assuming that ρ is proportional to $1/T$ the densities are obtained from the temperature field, without invoking the Boussinesq-type approximations.

3.2. *The solution procedure*

The above equations were solved on a square mesh by the finite-domain method outlined in refs. [16–18]. Finite-domain equations are derived by integration of the differential equations over an elementary control volume or cell surrounding a grid node. Upwind differencing is used in the convective terms and the integrated source term is linearized. Both these practices are widely used to enhance numerical stability. The upwind scheme has come under much criticism recently, but it is only grid-refinement that can detect the 'false diffusion' associated with the various schemes. Therefore, care was taken to obtain grid-independent results. Pressures are obtained from a pressure-correction equation which yields the pressure change needed to procure velocity changes to satisfy mass continuity. The 'SIMPLEST' practice [17] is followed for the momentum equations. The most significant difference between 'SIMPLEST' and the well-established 'SIMPLE' algorithm [19] is that in the former the finite-domain coefficients for momenta contain only diffusion contributions, the convection terms being added to the linearized source term of the equations. This implies that, in the absence of diffusion, the momentum equations are solved by a Jacobi point-by-point procedure as opposed to the more popular 'simultaneous' line-by-line procedures. This mixed practice (the use of Jacobi for convection terms, the use of line-by-line for diffusion terms) derives from experience and intuition. For example, use of Jacobi for diffusion in a pipe would take an extremely long time to spread the viscous effects of the wall, while a simultaneous solution would do that in virtually a single iteration. This is not so for the convection terms, however, because of their special links with the pressure-correction equation. The above mixed practice was found to accelerate convergence significantly.

The equations are solved by a line-by-line procedure which is similar to Stone's Strongly Implicit Method but free from parameters requiring case-to-case adjustment and so less complex and slower. The pressure-correction equation is solved in a 'whole-field' manner, 2-D simultaneous. Further details may be found in refs. [16, 17].

3.3. *The Nusselt number*

From the engineering viewpoint, the most important characteristic of the flow is the rate of heat transfer across the cavity. The Nusselt number on the hot wall at $y = 0$ is given by

$$Nu(z) = \left(\frac{\partial \theta}{\partial \bar{y}}\right)_{\bar{y}=0} = \left(\frac{\partial T}{\partial y}\right)_{y=0} \frac{D}{T_H - T_C}; \tag{8}$$

$$\left(\frac{\partial T}{\partial y}\right)_{y=0} = \frac{\dot{q}''_{\text{wall}}}{\kappa}; \tag{9}$$

$$Nu(z) = \frac{\dot{q}''_{\text{wall}}}{\kappa} \frac{D}{T_H - T_C}; \tag{10}$$

where the heat flux at the wall, $\dot{q}''_{\text{wall}}$, is calculated by the program, from wall-functions [12, 19].

The average Nusselt number is given by

$$\overline{Nu} = \int_0^1 \left(\frac{\partial \theta}{\partial \bar{y}}\right) \mathrm{d}z \,|_{\bar{y}=0 \text{ or } 1} \simeq \frac{1}{N} \sum_{j=1}^{N} \frac{\partial \theta}{\partial \bar{y}}(0, \bar{z}_j). \tag{11}$$

The mid-plane value $Nu_{1/2}$ is also computed as it is probably [3] a more accurate quantity in describing the heat flow across a cavity with adiabatic 'end' walls. The three- and five-point formulae commonly used by other investigators [20] for resolving the wall temperature gradient in equation (8) were also used. The five-point formula gave results very close to the ones calculated by equation (10) for Ra up to 10^8, but it became erroneous, as expected, for the high Ra numbers.

4. RESULTS AND DISCUSSION

The main results are presented in graphical and tabular form, and as Nu vs Ra correlations. The graphical results are obtained by the post-processor GRAFFIC [21].

Solutions were computed for $Pr = 0.71$ (air) and Ra between 10^3 and 10^{16}. The solutions for Ra up to 10^6 were obtained by using normalized variables, in such a way that dimensionless velocities were of the order of unity, in order to improve the numerical accuracy of the results. Indeed it was found that this procedure led to a 3% improvement in the important parameters over the dimensional solution, due to the limited accuracy of the mini-computer used.

The validity of the relationship $\theta(y, z) = \theta(1-y, 1-z)$, where θ is the dependent variable, was found to hold for all the solutions obtained, with very close approximation, everywhere in the flow field. An exception to this was in the cavity core for $Ra > 10^{12}$, probably due to the round-off error in the very small velocities encountered in this region, as compared with the large ones at the wall boundary layers; but even then the departure from the above centro-symmetry was within a few percent.

The presented results are practically grid independent (see Section 6 on grid dependence).

The velocity components at the domain centre-lines are shown in non-dimensional form (using κ/D as a scale factor, where κ is the thermal diffusivity) in Figs. 2–4, for Rayleigh numbers $Ra = 10^3$, 10^5 and 10^6.

It can be seen from these graphs that as the Rayleigh number increases, the velocity maximum moves closer to the wall and its amplitude increases. At the same time, the velocity between the two maxima becomes progressively smaller and at $Ra > 10^6$ flow reversal is observed immediately outside the boundary layers. The reason for the above behaviour will be explained in conjunction with the thermal distribution inside the section.

Figure 5 shows streamlines for $Ra = 10^3$–10^{16}. Corresponding maps of temperature are shown in Fig. 6. The presented contours, in all the figures are labelled according to a well-known convention. For example, in Fig. 6 the contours are labelled via the statement 283(2)303 K. This means that temperature contours are presented every 2 K with the first (at the extreme right) corresponding to 283 K and the last to 303 K.

At $Ra = 10^3$, streamlines are those of a single vortex, with its centre in the centre of the domain. Corresponding isotherms are parallel to the heated walls, indicating that most of the heat transfer is by heat conduction. The effect of convection is seen as the departure of the isotherms from the vertical. The vortex is generated by the horizontal temperature gradient

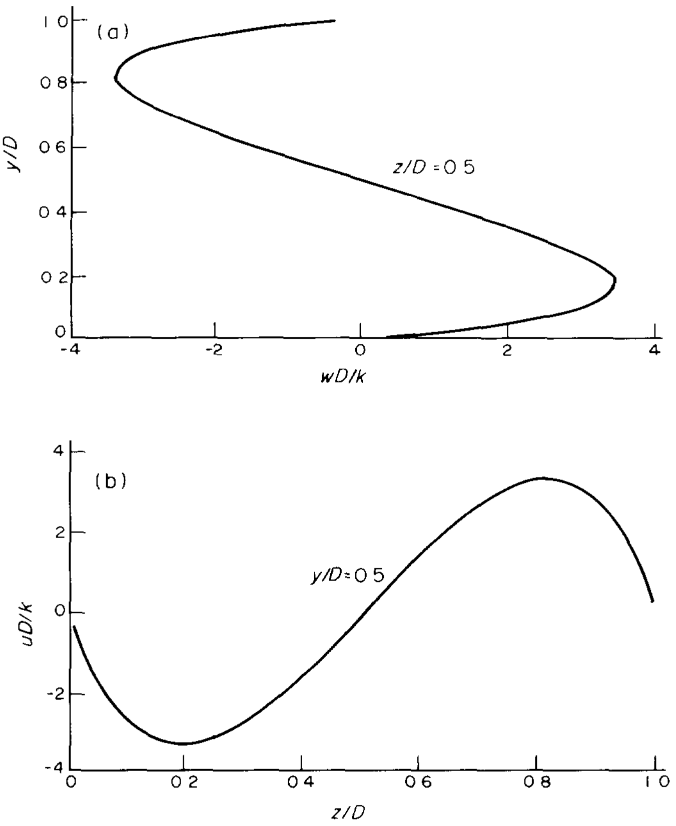

Fig. 2. (a) The vertical velocity component: $Ra = 10^3$. (b) The horizontal velocity component: $Ra = 10^3$.

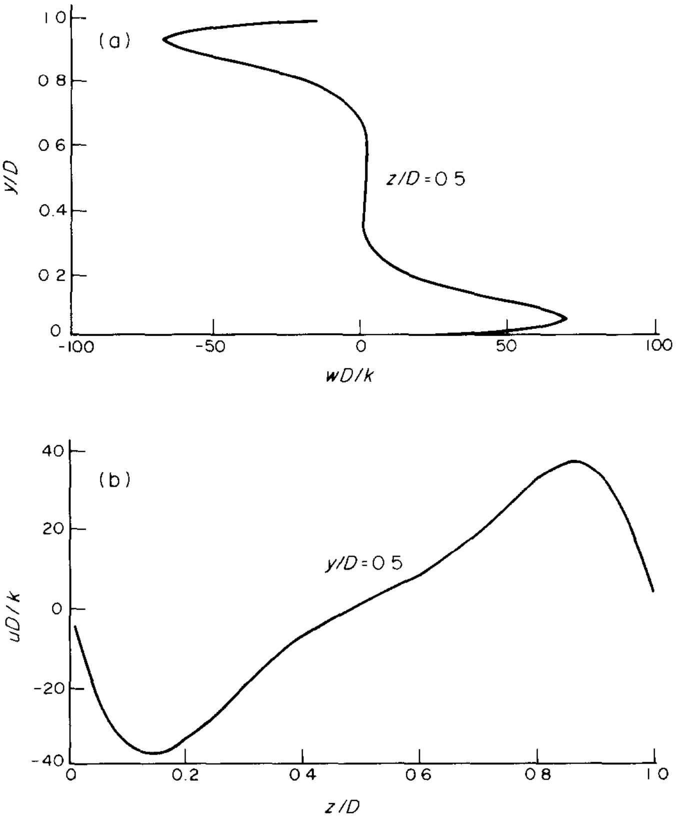

Fig. 3. (a) The vertical velocity component: $Ra = 10^5$. (b) The horizontal velocity component: $Ra = 10^5$.

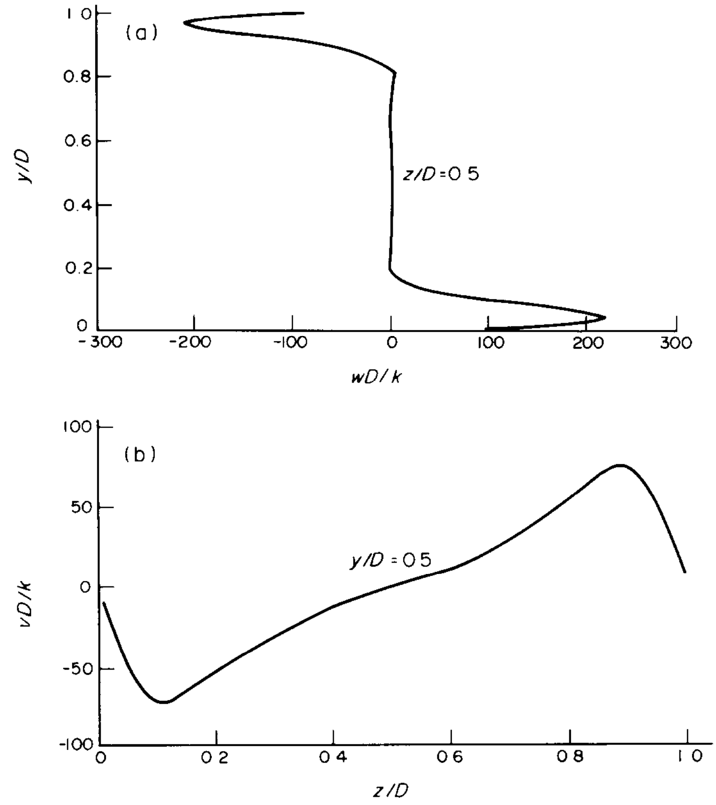

FIG. 4. (a) The vertical velocity component: $Ra = 10^6$. (b) The horizontal velocity component: $Ra = 10^6$.

across the section. This gradient, $\partial T/\partial y$, is negative everywhere in this case, giving rise to positive (clockwise rotation) vorticity.

As the Rayleigh number increases ($Ra = 10^4$) the central streamline is distorted into an elliptic shape and the effect of convection is more pronounced in the isotherms. Temperature gradients are now more severe near the vertical walls, but diminish in the centre. This behaviour continues to $Ra = 10^5$; the central streamline is further elongated and two secondary vortices appear inside it. Its long axis is now tilted in the direction of the flow, as the secondary vortices are convected by the flow in the periphery. Heat transfer by convection in the viscous boundary layers alters the temperature distribution to such an extent that temperature gradients in the centre are close to zero, or change sign, thus promoting negative vorticity. This causes the development of secondary vortices in the core.

As discussed in ref. [22], the secondary vortices in the square cavity do not result from an instability of the base flow but are a direct consequence of the convective distortion of the temperature field. As Ra increases, the development of thermal boundary layers intensifies $\partial T/\partial y$ in the vicinity of the walls, and the convection within each layer leads to negative $\partial T/\partial y$ in the centre. A vorticity sink thus separates the regions of concentrated vorticity generation and two secondary vortices are formed. Viscous diffusion appears to prohibit the development of these vortices for $Ra < 10^5$. The vortices at $Ra = 10^5$ are sufficiently strong to convect the temperature fields to the extent that the isotherms are nearly horizontal in the centre, preventing any vertical motion there (see w-velocity plots in Fig. 3).

Increasing Ra to 10^6, causes the secondary vortices to move closer towards the walls and are convected further downstream. A third vortex appears in the centre of the section, again rotating clockwise. This is surprising, as one would expect this last vortex to rotate counterclockwise, to reduce the shear between the other two vortices. Mallinson and de Vahl Davis [22] attribute this to the presence of a small positive temperature gradient in the centre. Viscous diffusion between the secondary vortices dissipates any counterclockwise vortices that might appear. Heat transfer is now mostly by convection in the rapidly moving fluid near the walls. The boundary layers adjacent to the vertical walls have become thin and fast. In the central region the vertical stratification in the temperature distribution, shown in Fig. 6 with increasing values from the bottom to the top of the cavity, prevents any vertical motion as confirmed by the w-plots in Fig. 4. In general, as Ra is increased w tends to become comparatively small outside the vertical boundary layers, and is virtually zero over the central

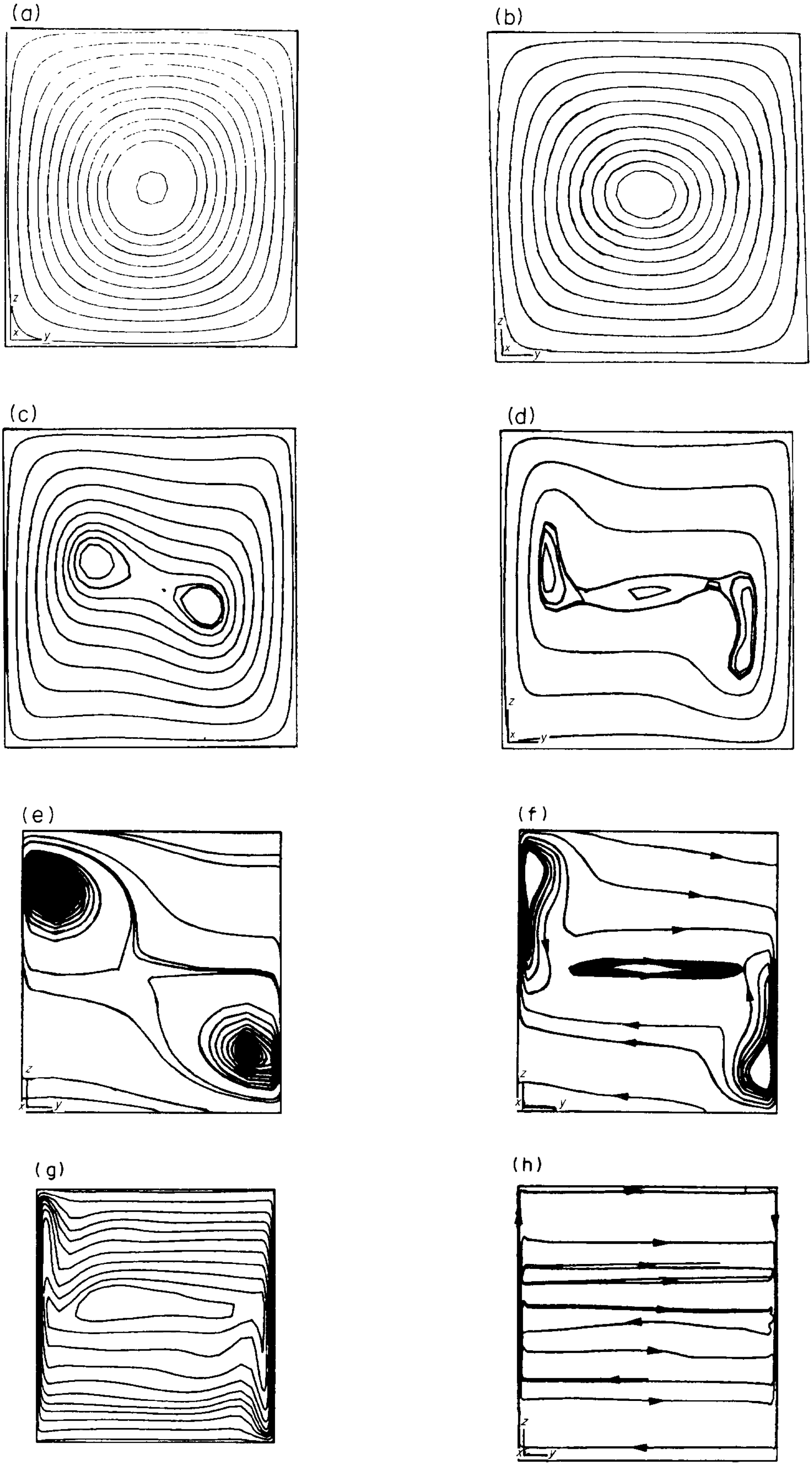

FIG. 5. Streamlines: (a) $Ra = 10^3$; (b) $Ra = 10^4$; (c) $Ra = 10^5$; (d) $Ra = 10^6$; (e) $Ra = 10^8$; (f) $Ra = 10^{10}$; (g) $Ra = 10^{12}$; (h) $Ra = 10^{16}$.

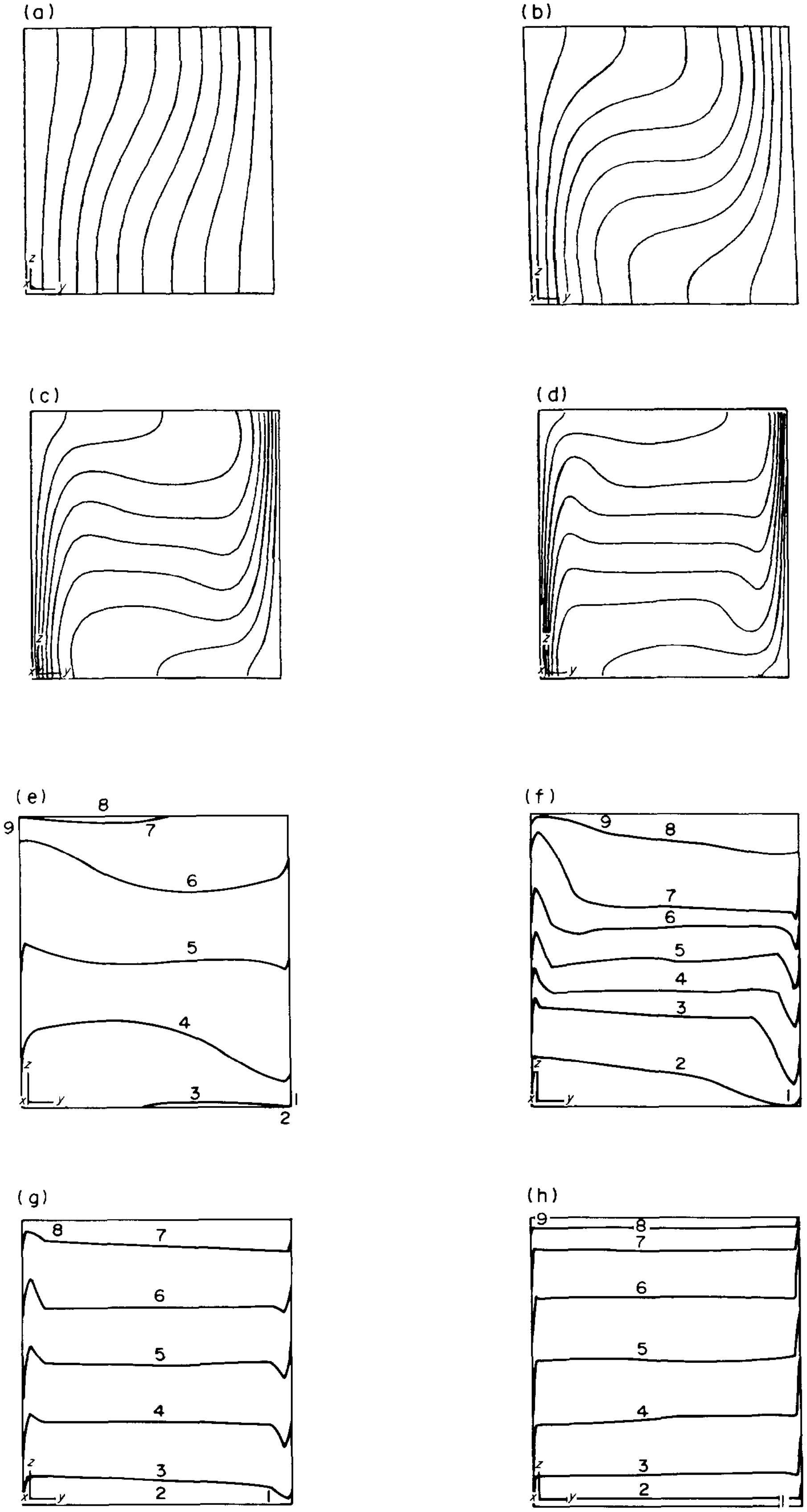

FIG. 6. Isotherms: (a) $Ra = 10^3$; (b) $Ra = 10^4$; (c) $Ra = 10^5$; (d) $Ra = 10^6$; (e) $Ra = 10^8$; (f) $Ra = 10^{10}$; (g) $Ra = 10^{12}$; $Ra = 10^{16}$. Contours at 283(2)303 K, except (f) which is at 288(1)298 K.

60% of the cavity width at $Ra = 10^6$. The maximum and minimum w values for each profile are strongly affected by the Ra number as shown in Table 1. In this table (and also in Table 2) the velocities are normalized using D as a scale factor for length and D^2/κ as a scale factor for time. The results obtained for $Ra = 10^6$ were identical whether the $(k \sim \varepsilon)$ model was used or not, due to virtually zero k generation.

As the Ralyeigh number increases from 10^6 to 10^8, the secondary vortices generated in the central core, are convected further upstream and closer to the differentially heated walls. The central vortex has now diffused into the other two vortices which become a dominant feature of the flow. The boundary layers on the heated walls are now very thin. At the upstream corner of each boundary layer, the low momentum outer layer is absorbed by the adjacent vortex, while the rest of the boundary layer follows the adiabatic wall under the action of the secondary vortices.

For $Ra = 10^{10}$ the central vortex reappears [Fig. 5(f)] and the other two vortices are shifted closer to the walls and get thinner and elongated. As Ra increases further, the vortex system becomes progressively weaker and eventually $(Ra = 10^{16})$ disappears completely. High velocities now only occur within the thin boundary layers, and the flow in the central core is stratified. The streamline patterns of Fig. 5(h) show this feature very clearly. Recirculation now only exists within the isothermal layers of fluid and the sense of rotation alternates between adjacent layers.

The accompanying temperature maps, for $Ra = 10^8$ and 10^{10} show the temperature range in the core diminishing, from between 289 and 297 K to 291 and 295 K. A steep temperature gradient accompanies the location of the secondary vortices. The horizontal extent and magnitude of this gradient determines the extent and strength of the vortices described earlier. The negative temperature gradient in the central vortex is observed. For high Ra, the T-profiles have a very steep slope within the thermal boundary layers; and this becomes steeper as Ra increases. Outside the boundary layers the T-profiles are almost horizontal and temperature increases with z.

Surprisingly, as the Rayleigh number increases even further, the temperature range in the core increases again, to between 288 and 298 K $(Ra = 10^{12})$ and finally to 287 and 299 K at $Ra = 10^{16}$. This is due to weak interchange of heat and momentum between adjacent fluid layers as the flow becomes increasingly stratified. At the same time, the temperature gradient in the horizontal direction diminishes to zero. This is to be expected, since now the walls are 'too far away' to have any influence in the core $(Ra \propto D^3$, while $\delta \propto D^{-3/4})$.

Figures 7 and 8 show horizontal and vertical velocity contours at various Ra numbers. For Rayleigh numbers up to 10^6 these contours are normalized, but not for the higher ones. The main observations discussed so far can also be inferred from these figures, i.e. the location and thickness of the boundary layers and the location of reverse flow regions accompanying

Table 1. Summary of the important quantities

Ra	10^3	10^4	10^5	10^6	10^8	10^{10}	10^{12}	10^{14}	10^{16}
$v_{max}(\bar{y} = 0.5)$	3.544	16.18	35.73	68.81	514.3	2.323×10^3	1.289×10^4	6.114×10^4	2.208×10^5
$\bar{z}$	0.832	0.832	0.857	0.872	0.941	0.9625	0.9925	0.996	0.997
$w_{max}(\bar{z} = 0.5)$	3.593	19.44	69.08	221.8	1812	1.689×10^4	1.156×10^5	1.134×10^6	9.42×10^6
$\bar{y}$	0.168	0.113	0.067	0.0375	0.0135	0.0055	0.00225	7.5×10^{-4}	2.55×10^{-4}
v_{max}	3.544	16.18	42.51	117.8	1409	1.0×10^4	5.103×10^4	3.495×10^5	1.238×10^6
$(\bar{y}, \bar{z})$	(0.5, 0.832)	(0.5, 0.832)	(0.2745, 0.894)	(0.1687, 0.9547)	(0.11, 0.987)	(0.065, 0.9928)	(0.0175, 0.9985)	$(4.19 \times 10^{-3}, 0.9995)$	$(7.5 \times 10^{-4}, 0.9999)$
w_{max}	3.593	19.44	69.08	226.7	1918	1.718×10^4	1.269×10^5	1.179×10^6	1.034×10^7
$(\bar{y}, \bar{z})$	(0.168, 0.5)	(0.113, 0.5)	(0.067, 0.5)	(0.0378, 0.451)	(0.0165, 0.732)	(0.0055, 0.421)	(0.00179, 0.3179)	$(7.5 \times 10^{-4}, 0.594)$	$(2.67 \times 10^{-4}, 0.2865)$
Nu_{max}	1.496	3.482	7.626	17.872	61.06	361.47	2007.8	9163.8	39 353.9
$\bar{z}$	0.0825	0.1425	0.0825	0.0375	0.0075	0.001	3×10^{-4}	9.99×10^{-5}	3×10^{-5}
$\overline{Nu}$	1.108	2.201	4.430	8.754	32.045	156.85	840.13	3624.4	11 226
Nu_{min}	0.720	0.643	0.824	1.232	5.2246	23.462	94.889	252.93	740.56
$\bar{z}$	0.9925	0.9925	0.9925	0.9925	0.997	0.9988	0.9997	0.9998	1.0

Table 2. Comparison of the two solutions

	Ra							
	10^3		10^4		10^5		10^6	
	1	2	1	2	1	2	1	2
$v_{\max}$	3.544	3.649	16.18	16.178	35.73	34.73	68.81	64.63
$\bar{z}$	0.832	0.813	0.832	0.823	0.857	0.855	0.872	0.850
$w_{\max}$	3.593	3.697	19.44	19.617	69.08	68.59	221.8	217.36
$\bar{y}$	0.168	0.178	0.113	0.119	0.067	0.066	0.0375	0.0379
$\overline{Nu}$	1.108	1.118	2.201	2.243	4.430	4.519	8.754	8.799
$Nu_{\max}$	1.496	1.505	3.482	3.528	7.626	7.717	17.872	17.925
$\bar{z}$	0.0825	0.092	0.1425	0.143	0.0825	0.081	0.0375	0.0378
$Nu_{\min}$	0.720	0.692	0.643	0.586	0.824	0.729	1.232	0.989
$\bar{z}$	0.9925	1.0	0.9925	1.0	0.9925	1.0	0.9925	1.0

Note: (1) Present solution; (2) de Vahl Davis' solution [3].

the secondary vortices. The vertical velocity maximum moves closer to the hot wall as the Rayleigh number increases, and it is close to the centre of the hot wall for Rayleigh numbers up to 10^6 (see also Table 1). The maximum horizontal component also moves closer to the hot wall as the Rayleigh number increases, and is shifted upwards.

Figure 9 shows the resulting velocity fields. The boundary layer profiles and the diminishing velocity field in the centre are clearly seen. An enlarged view of the central portion of Fig. 9(d) (indicated by the dotted line) shows clearly the presence and direction of the three secondary vortices (Fig. 10).

Figure 11 presents boundary layer velocity profiles at the 'hot' wall for $Ra = 10^{12}$, at various $\bar{z}$-locations. The boundary layer gets progressively thicker as we move from the bottom ($IZ = 15$, $\bar{z} = 0.0075$) up to $z = 0.5$. Further up, $\bar{z} = 0.795$, negative flow is observed at the edge of the boundary layer, which is now thinner. The reason for this was explained earlier in connection with the presence of the secondary vortices. The boundary layer at $\bar{z} = 0.9925$ has almost disappeared as it approaches separation at the top corner. Inspection of the detailed results indicates that both velocity components are indeed negative at that corner. The velocity profiles within the boundary layers are not logarithmic in nature (neglecting the near-wall points where a logarithmic profile was imposed by the use of the 'wall functions'). This is in agreement with the results of George and Capp [27].

Figure 12 presents w-velocity profiles within the narrow boundary layer near to the hot wall, for $Ra = 10^{10}$ with two different scaling factors. Three profiles are presented at three horizontal stations, $z/D = 0.25$, 0.50 and 0.75. Figure 13 presents the same information for $Ra = 10^{12}$.

The important quantities for the problem considered, e.g. the Nusselt numbers and the maximum velocities are summarized in Table 1. The table shows the calculated Nusselt numbers at the 'hot' wall.

The maximum and minimum values are given in the table, together with the Nusselt number at $\bar{y} = y/D = 0.5$. The same table, contains values of the maximum vertical velocity component on the horizontal mid-line and its location, the maximum horizontal velocity on the vertical mid-line and its location and the maximum horizontal and vertical velocities over the whole domain and their location.

The heat transfer coefficient is seen to increase with Rayleigh number, as convection becomes dominant, but not as fast as the flow. Thus, passing from $Ra = 10^3$ to 10^6 leads to an increase of $w_{\max}$ from 3.59 to 221.8;

Table 3. Comparison of present and experimental correlations (arrows indicate range of validity of equations used)

	Nu (laminar)			*Nu* (turbulent)		
log *Ra*	Equation (12)	Equation (20)	Δ%	Equation (14)	Equation (21)	Δ%
3	1.128	1.102	+2.4	—	—	—
4	2.246	1.960↑	+14.6	1.698	1.546	+9.8
5	4.470	3.485	+28.3	3.621	3.329↓	+8.8
6	-	—	—	7.723	7.167↑	+7.2
8	—	--	—	35.14↓	33.40	+5.2
10	—	—	—	159.9	155.0	+3.1
12	—	—	—	727.5	720.0	+1.0

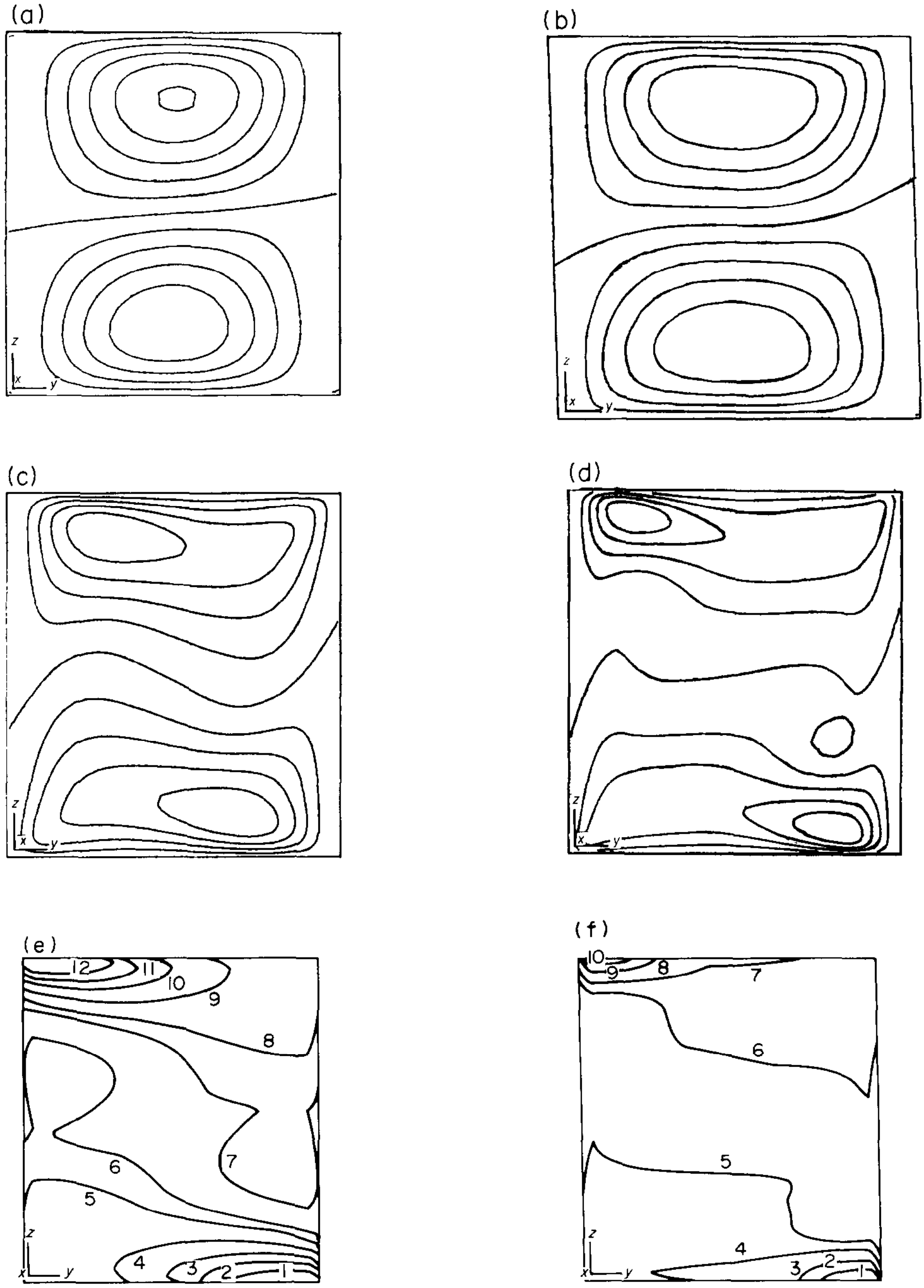

FIG. 7. Horizontal velocity (v) contours: (a) $Ra = 10^3$, contours at $-3.55(0.711)3.55$; (b) $Ra = 10^4$, contours at $-16(3.2)16$; (c) $Ra = 10^6$, contours at $-43(8.62)43$; (d) $Ra = 10^6$, contours at $-117.88(23.58)117.88$; (e) $Ra = 10^8$, contours at $\pm 0.005, 0.01, 0.02, 0.03, 0.04, 0.05$; (f) $Ra = 10^{10}$, contours at $\pm 0.01, 0.025, 0.05, 0.075, 0.1$.

but the maximum Nusselt number increases only from 1.496 to 17.87, despite the passage from diffusion-dominated to convection-dominated transfer, as revealed by the configuration of the isotherms.

The maximum Nusselt number occurs at the bottom of the cavity and the minimum at the top.

The results for Rayleigh numbers up to 10^6 are compared with the benchmark solution provided in ref. [3] which can be considered as accurate. The qualitative agreement of the presented plots of stream function, temperature and velocity maps with those of the benchmark solution is very good. Quantitative comparison is provided by the Nusselt numbers and the maximum velocity values in Table 2. Agreement is generally good. Differences exist in the minimum Nusselt number, particularly at $Ra = 10^6$. Although the agreement of the maximum and centre-line Nusselt numbers is better than 1.5% over the whole Ra range, the present predictions indicate a higher minimum Nusselt number than the benchmark solution.

Numerical errors and the first-order differencing scheme used in this work do not account for the observed differences, since the results are practically grid independent. However, there are two other

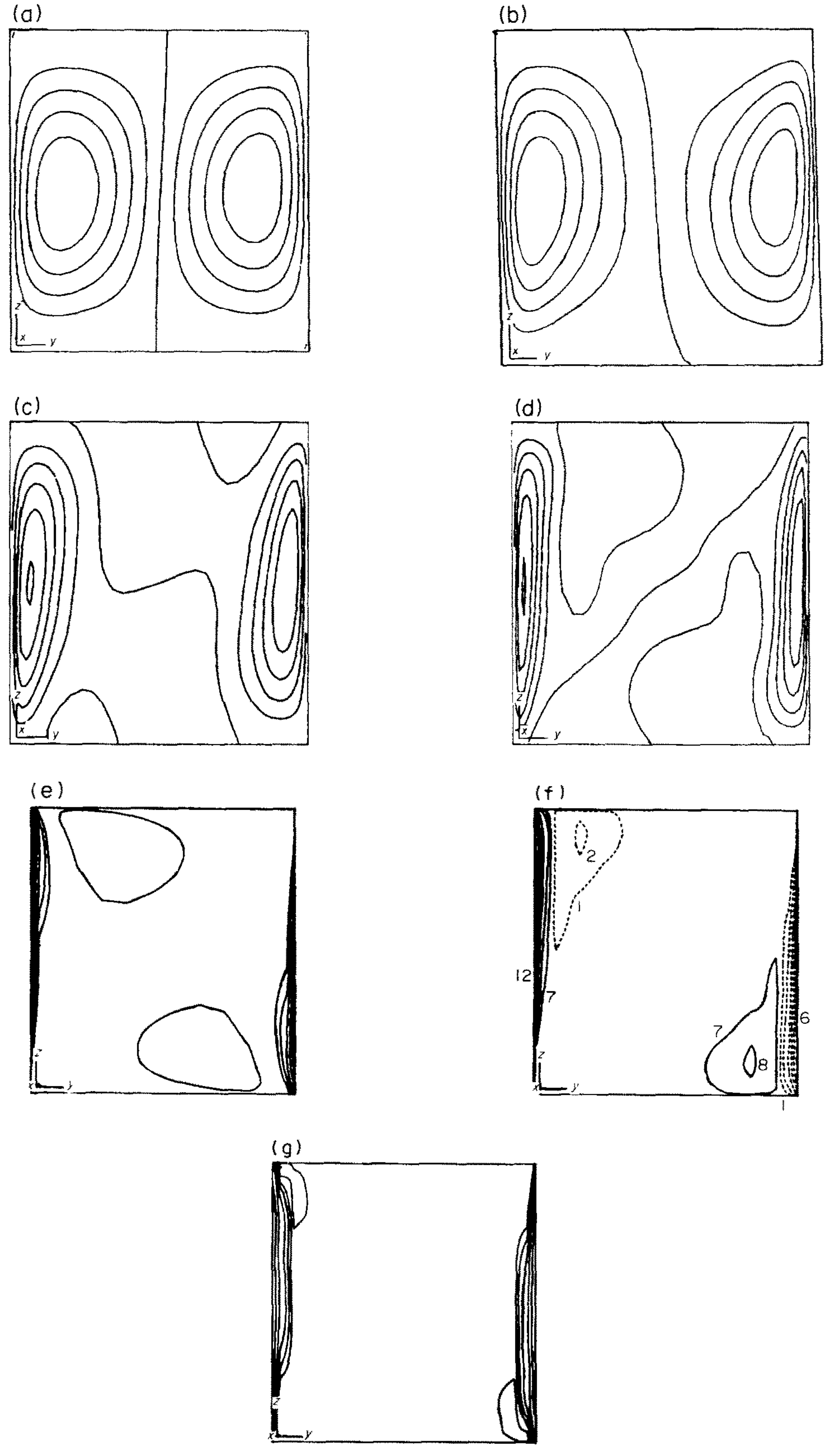

FIG. 8. Vertical velocity (w) contours: (a) $Ra = 10^3$, contours at $-3.555(0.711)3.555$; (b) $Ra = 10^4$, contours at $-19.24(3.848)19.24$; (c) $Ra = 10^5$, contours at $-67.55(13.51)67.55$; (d) $Ra = 10^6$, contours at $-217.38(43.47)217.38$; (e) $Ra = 10^8$, contours at $\pm 0.0075, 0.0125, 0.02, 0.03, 0.04, 0.05, 0.06$; (f) $Ra = 10^{10}$, ——— >0, ---- <0, contours at $\pm 0.01, 0.025, 0.05, 0.075, 0.1, 0.15$; (g) $Ra = 10^{12}$, contours at $\pm 0.01, 0.025, 0.05, 0.1, 0.2$.

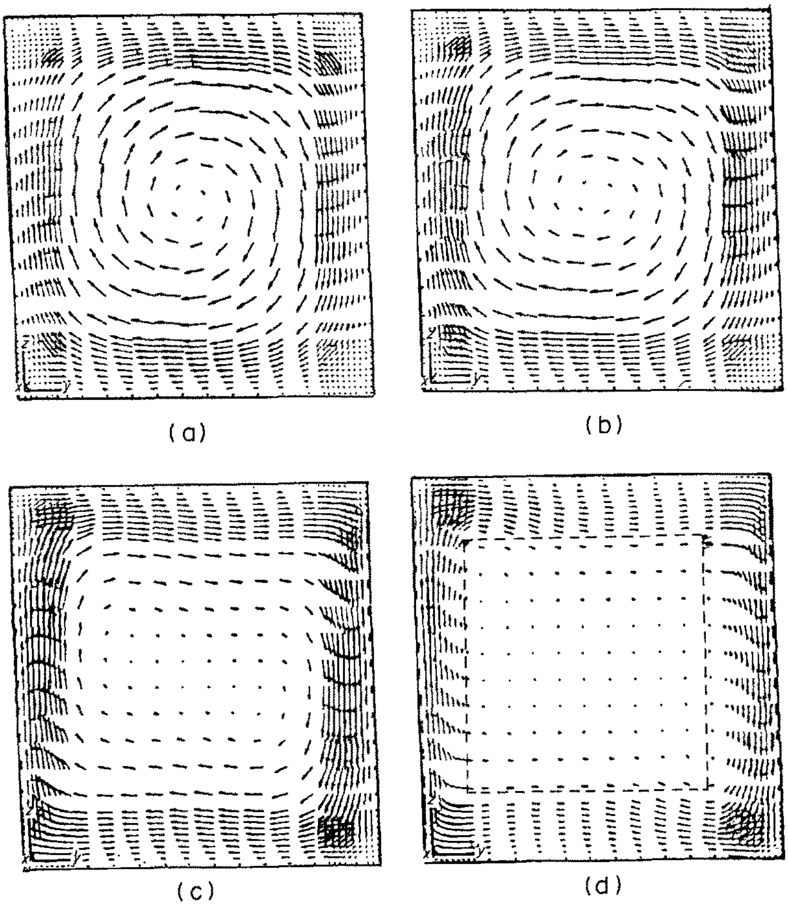

FIG. 9. Vector fields: (a) $Ra = 10^3$; (b) $Ra = 10^4$; (c) $Ra = 10^5$; (d) $Ra = 10^6$.

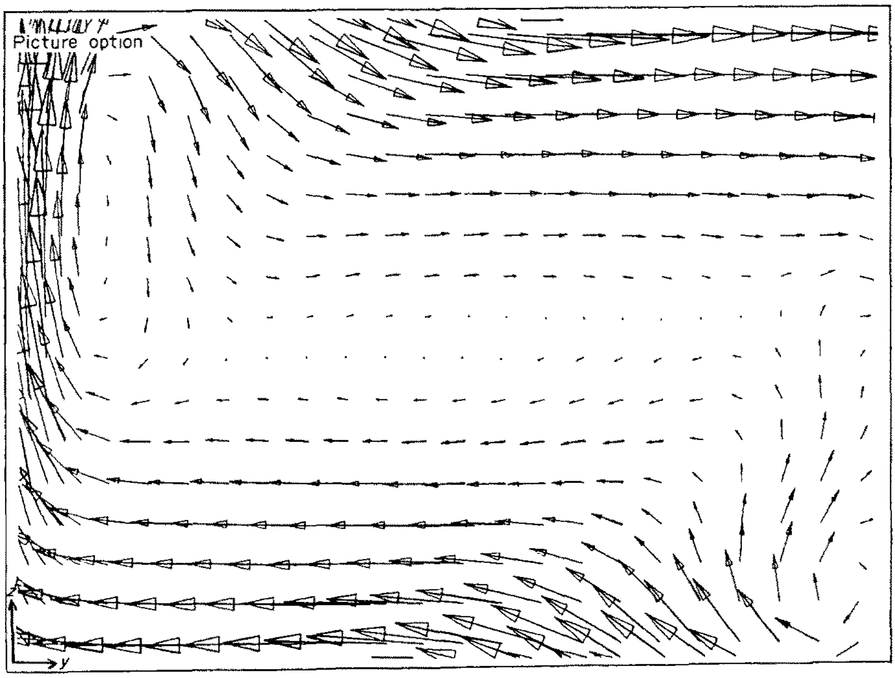

FIG. 10. Secondary vortices at $Ra = 10^6$.

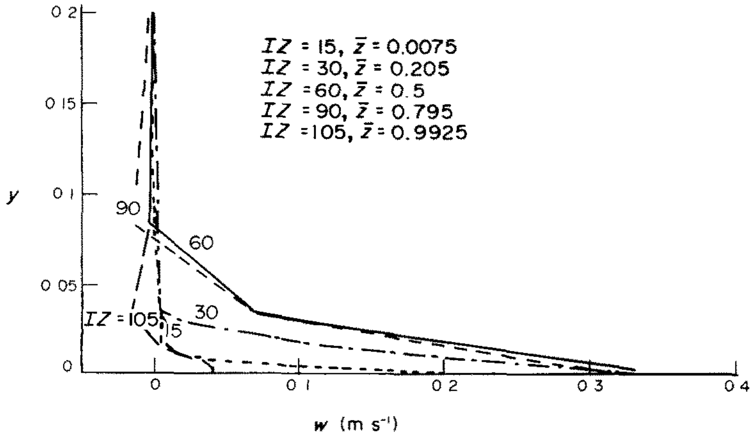

FIG. 11. Boundary layer velocity profiles at $Ra = 10^{12}$, 'hot' wall.

differences between the procedures, namely the elimination of the Boussinesq assumption in the present work and the implied use of the linear velocity profile between wall and near-wall points, in the shear-stress calculation. The latter should not account for any difference either, provided that the benchmark solution has properly computed the wall shear-stresses.

The computations were repeated by using the Boussinesq approximation. Minor differences were observed for $Ra = 10^3$ and 10^4, with a maximum of 1%. For $Ra = 10^5$ and 10^6 the differences were up to 3.7%; the minimum Nusselt number being 0.804 at $Ra = 10^5$ and 1.188 at $Ra = 10^6$. The large errors in the calculation of the minimum Nusselt number appear to be due to the sensitivity of its calculation. Suppose for example that at $Ra = 10^6$ the solution predicts a near-wall maximum temperature of 302.81 K instead of the correct value of, say, 302.84 K. This represents a very accurate temperature prediction with an error of less than 0.01% (well within the convergence criterion used, see Section 5). For a wall temperature of 303 K, the application of a one-sided formula for calculating a temperature gradient at the wall, would lead to a $Nu_{\min}$ which for the present grid spacing would be 1.267 instead of 1.067, e.g. in error by 19%. The same is not true in the case of $Nu_{\max}$. Thus the same accuracy in temperature (say 300.43 K instead of 300.4 K) leads to $Nu_{\max} = 17.13$ instead of 17.33, e.g. in error by only 1%. Therefore, despite the large errors at $Ra = 10^6$ in the derived quantities, it is suggested that the present

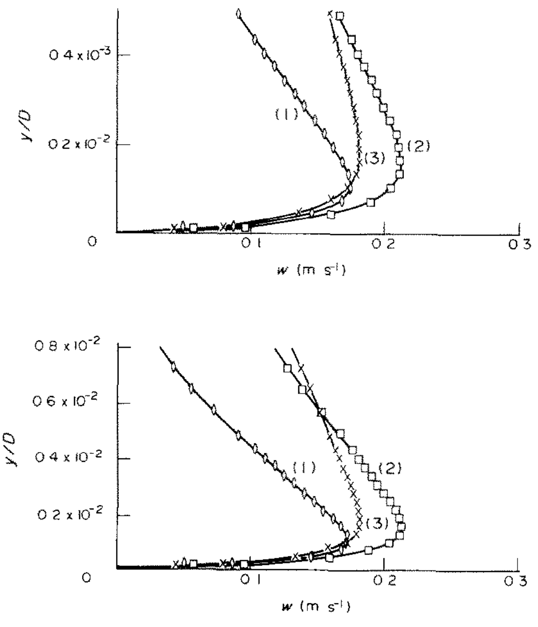

FIG. 12. w-Velocity profiles within boundary layer, $Ra = 10^{10}$ (two scaling factors). Three horizontal stations at: (1) $z/D = 0.25$; (2) $z/D = 0.50$; (3) $z/D = 0.75$.

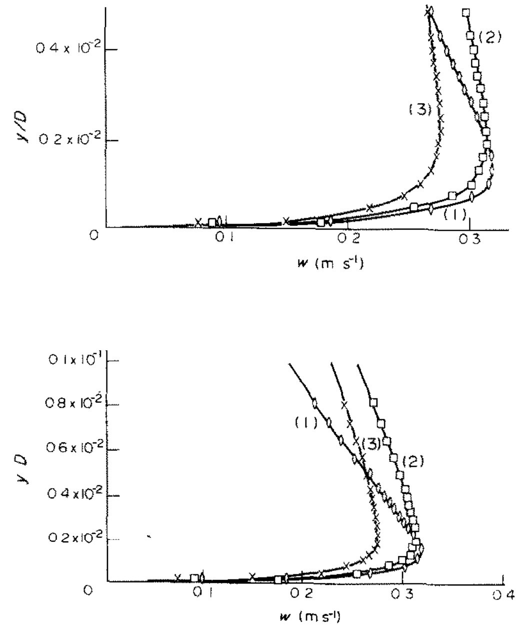

FIG. 13. w-Velocity profiles within boundary layer, $Ra = 10^{12}$ (two scaling factors). Three horizontal stations at: (1) $z/D = 0.25$; (2) $z/D = 0.50$; (3) $z/D = 0.75$.

solution may still be about 1% accurate in terms of the computed primitive variables.

Direct comparisons are not possible for the turbulence runs, due to the scarcity of experimental evidence. However, the use of the $k \sim \varepsilon$ model in other related work (e.g. buoyant turbulent flow in buildings) has led to favourable comparisons with experiment [15].

Furthermore, the presented solutions certainly show some of the features that are observed experimentally (position of vortices and their shifting with increasing *Ra* number, thermal stratification, etc.) and indicate, qualitatively at least, the correct change in flow structure as *Ra* increases.

Finally, the correlations of the present results given below are in good agreement with well-known correlations derived from a large number of experiments for *Ra* up to 10^8 [23], and appear to extend the validity of those correlations up to $Ra = 10^{12}$. For higher *Ra* a set of new correlations is proposed.

4.1. *Derived Nu ~ Ra correlations*

The following correlations for maximum, minimum and average Nusselt numbers were derived from the present predictions by least-square linear regression.

Laminar ($10^3 \leqslant Ra \leqslant 10^6$)

$$Nu_{1/2} = \overline{Nu} = 0.143Ra^{0.299}; \qquad (12)$$

$$Nu_{\max} = 0.130Ra^{0.356}. \qquad (13)$$

The minimum *Nu* is not given as the log *Nu* vs log *Ra* curve is not a straight line.

Turbulent ($10^6 < Ra \leqslant 10^{12}$)

$$\overline{Nu} = 0.082Ra^{0.329}; \qquad (14)$$

$$Nu_{\max} = 0.057Ra^{0.379}; \qquad (15)$$

$$Nu_{\min} = 0.016Ra^{0.315}. \qquad (16)$$

Turbulent ($10^{12} < Ra \leqslant 10^{16}$)

$$\overline{Nu} = 1.325Ra^{0.245}; \qquad (17)$$

$$Nu_{\max} = 0.34Ra^{0.316}; \qquad (18)$$

$$Nu_{\min} = 0.137Ra^{0.233}. \qquad (19)$$

4.2. *Comparison with experimental correlations*

The above correlations are compared with the following experimental ones in Table 3 [23]:

laminar

$$\overline{Nu} = 0.196Ra^{1/4}\left(\frac{L}{D}\right)^{-1/9}$$

$$(2.8 \times 10^3 < Ra < 2.8 \times 10^4); \qquad (20)$$

turbulent

$$\overline{Nu} = 0.072Ra^{1/3}\left(\frac{L}{D}\right)^{-1/9}$$

$$(2.8 \times 10^4 \leqslant Ra \leqslant 1.55 \times 10^7); \qquad (21)$$

where L/D is the cavity aspect ratio.

It can be seen that extrapolation of the experimental turbulence correlation up to Rayleigh numbers of 10^{12} is in good agreement with the present predictions, despite the fact that the former is applicable to cavities of aspect ratios between 3 and 42. The aspect-ratio effect explains the relatively large differences observed for the lower *Ra* numbers, and the closer agreement obtained for higher *Ra* numbers; the effect of aspect ratio diminishes as *Ra* increases.

The switch in the exponent of the Rayleigh number for the correlations for $Ra > 10^{12}$ was introduced simply by requiring a zero error from the least-square linear regression. Experimental evidence, however limited, indicates an exponent of 1/3. If the exponent of *Ra* is assumed to be 1/3, then the best correlation of the present results over the whole of the turbulent range gives

$$\overline{Nu} = 0.060Ra^{1/3}. \qquad (22)$$

The above correlation gives higher values than those obtained by MacGregor and Emery ($\overline{Nu} = 0.046Ra^{1/3}$) [28] and by Cowan *et al.* ($\overline{Nu} = 0.043\ Ra^{1/3}$) [26]. However, the former [28] refers to cavities of aspect ratio 10–40 with constant heat flux boundary conditions at the hot face, and isothermal cold face and the latter [26] refers to water and to *Ra* numbers up to 2×10^{11}.

5. CONVERGENCE AND COMPUTER TIME

A converged solution was defined as one that met the following criterion for all dependent variables

$$\max|\phi^{n+1} - \phi^n| \leqslant 10^{-4},$$

between sweeps n and $n+1$. At this stage mass continuity errors per slab were of the order of 10^{-8} and therefore insignificant. Further sweeps of the solution domain confirmed no changes and were actually pointless since the accuracy limit of the computer was approached. The sum of the absolute volumetric error over the whole field was again insignificant, at 10^{-6}.

Convergence was found to be affected by the Rayleigh number. Hence, the high Rayleigh number cases required more sweeps than the low ones. To improve convergence, a false time-step relaxation was used. This was reduced by an order of magnitude, from 0.1 to 0.01 for both velocities, for $Ra > 10^5$, and to 0.001 for $Ra > 10^{10}$. This is to be expected since this relaxation factor is proportional to the fluid residence time in a typical cell; and it is therefore appropriate to reduce it as the velocity in the boundary layers increases with Rayleigh number.

To economize on run-times each Rayleigh number case was restarted from the previous one (starting with $Ra = 10^3$) and 200 sweeps were found adequate for convergence. The domain dimension *D* was the parameter adjusted to get the required Rayleigh number value.

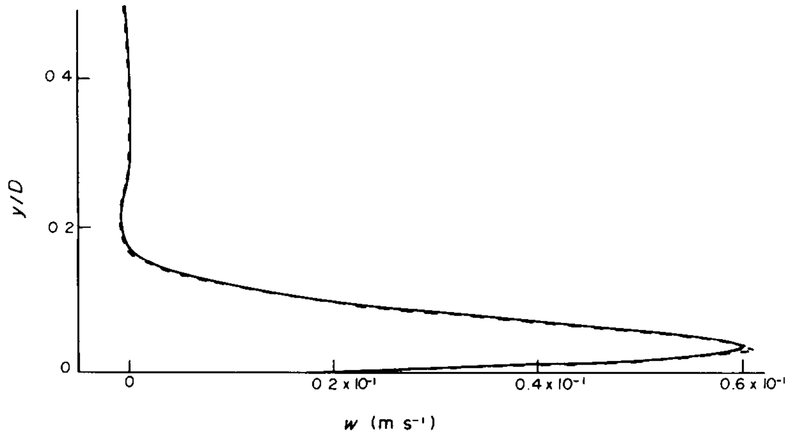

FIG. 14. Velocity comparison ($Ra = 10^6$) for 40 × 40 and 80 × 80 solutions.

A 100-sweep run required 11 min CPU time on the Perkin-Elmer 3220 mini-computer, for the 30 × 30 grid, and 15 min for a 40 × 40 grid. The above mini-computer is several times slower than mainframe machines. In general, the time per finite-domain cell, per sweep, per variable was 1.5×10^{-3} s CPU on the Perkin-Elmer machine. A full run at $Ra = 10^{14}$ using a 60 × 60 grid would require 300 sweeps and take 2.5 h on the mini-computer for solving the six equations $(v, w, p, k, \varepsilon, T)$.

It is not an easy matter to compare the above reported CPU times with those of other methods in the literature, because of different computers used and different practices in reporting these times.

However, it appears to the authors after their survey that the present computer-time requirements are modest, and possibly an order of magnitude less than those reported in the literature for the same cases. If true, this is certainly due to the speed of the SIMPLEST algorithm and the associated whole-field pressure solver, coupled with the thorough optimization of FORTRAN arithmetic and the very orderly bookkeeping in the software, embodying the solution procedure.

6. GRID DEPENDENCE AND COMPUTER STORAGE

Initial investigations were performed on a uniform 30 × 30 grid. This was found to be adequate for $Ra = 10^3$, but not for higher values. An improved 30 × 30 grid was then used, with closer spacing near the walls (Fig. 1), to increase boundary layer resolution.

This grid was used for all Rayleigh number cases up to $Ra = 10^6$ and the results were stored.

To check grid dependency, the grid was further refined to 40 × 40 by adding intermediate cells in the central region. All cases (up to $Ra = 10^6$) were re-run restarting from interpolation of the 30 × 30 results, for another 100 sweeps. In their bulk, the results showed little change, although the secondary vortices at $Ra = 10^5$ and 10^6 were, as expected, better resolved. The maximum velocity increased by 5% in the $Ra = 10^5$ case, and these are the results presented in this paper.

The grid was refined again to 80 × 80 by halving all cells and the $Ra = 10^6$ case was run for another 300 sweeps. Very minor changes were observed, as shown in Fig. 14, for the velocity profile inside the hot wall boundary layer. The maximum velocity increased by 0.4% in the $Ra = 10^6$ case. The same observations apply also to the temperature-field changes with grid refinement. It is concluded that the results up to $Ra = 10^6$ are practically grid-independent.

For the turbulent cases care was taken to place 10–15 grid cells inside the wall boundary layers. The thickness of these layers is given by $\delta/D = 4.86Ra^{-1/4}$ for $Pr = 0.71$. Care was also taken to concentrate several of these 10–15 points between the velocity peaks and the wall, and to place the first grid point very close to the wall ($y/D = 1 \times 10^{-6}$ for the high Ra numbers, y^+ varying between 1 and 12 along the hot wall). The above considerations are very important for treating the boundary layers in accordance with the essential physics, since in the wall region temperature gradients are most severe and hence provide an important source of vorticity. If the first grid point is too far from the wall then the results will be grossly distorted by this effect. Three grids were used, $(y, z) = 40 \times 80, 60 \times 120$ and 100×160. Practically grid-independent results seemed to be obtained using a grid of $(y, z) = 60 \times 120$ for all $Ra \geqslant 10^8$; the 100 × 160 grid leading to a maximum further change of 1.2% for the maximum velocities and 1.5% for temperature. For $Ra > 10^{14}$ the resulting grid cells in the core were thought to be too ill-conditioned (aspect ratio of up to 10:1) for sufficient accuracy. However, the flow in the core for these high Ra numbers is nearly stagnant and the cell aspect-ratio effect appears not to be important, as was indicated by repeating the runs with half the above ratios.

The program required 90 K-words; of these, 35 K-words were required for data storage (30 × 30 grid).

7. CONCLUSIONS

The problem considered represents a 2-D approximation to a series of practical problems. The study demonstrated that numerical solutions can be obtained quickly and economically for such problems, where buoyancy effects are dominant.

Accurate results were obtained at both ends of the Rayleigh number scale, at least for the laminar range, indicating that both diffusion-only or convection-only heat transfer problems can be tackled with ease. The results were presented in graphical and tabular form, and as correlations between the Nusselt and Rayleigh numbers.

The main points of the present method can be summarized as follows: (a) the model consists of the coupled differential elliptic equations which are solved over the entire flow domain, with no assumption concerning the core configuration; (b) the procedure is strongly convergent and results were easily obtained even at Rayleigh numbers as high as 10^{16}; (c) practically grid independent results were obtained with only modest computer storage and CPU time requirements. Indeed, a survey revealed that the present method may be up to an order of magnitude faster than other available procedures, enabling very fine grid runs to be performed within practicable resources; (d) the procedure and associated computer program are general and can be used immediately for 3-D natural convection problems in cavities of any aspect ratio and orientation, and fluids of any Prandtl number. It is therefore immediately applicable to all related practical problems; (e) the speculative use of the $(k \sim \varepsilon)$ model in this work has indicated that, despite its well-known deficiencies in terms of physical realism, it may still lead to a reasonable prediction of the overall flow structure of the problems considered; (f) apart from the uncertainty connected with the $(k \sim \varepsilon)$ model itself another source of uncertainty is provided by the 'wall-functions'. More work is required to establish more realistic 'wall-functions' for buoyancy-dominated flows. Once established, it is a very simple matter to incorporate in the present model.

Although only time-averaged steady-state results have been presented, the procedure can also be used in its in-built transient mode. Also radiation and variable property effects, that have been neglected in the present study, must be included to investigate their importance at high Rayleigh numbers. Finally, much more experimental work is required for high *Ra* numbers to provide data for improving and validating the computer models.

REFERENCES

1. I. P. Jones, A comparison problem for numerical methods in fluid dynamics: the 'double-glazing' problem, in *Numerical Methods in Thermal Problems* (edited by R. W. Lewis and K. Morgan), pp. 338–348. Pineridge Press, Swansea, U.K. (1979).
2. G. de Vahl Davis and I. P. Jones, Natural convection in a square cavity—a comparison exercise, *Int. J. Num. Methods Fluids* **3,** 227–248 (1983).
3. G. de Vahl Davis, Natural convection of air in a square cavity: a benchmark numerical solution, *Int. J. Num. Methods Fluids* **3,** 249–264 (1983).
4. I. Catton, Natural convection in enclosures, in *Heat Transfer 1978,* Vol. 6. National Research Council of Canada (1978).
5. S. Ostrach, Completely confined natural convection, *Developments in Mechanics, Proc. Tenth Midwestern Mechanics Conf.,* Vol. 4, pp. 53–81. Johnson, Chicago, Illinois (1967).
6. S. Ostrach, Natural convection in enclosures, in *Advances in Heat Transfer* (edited by J. P. Hartnett and T. F. Irvine, Jr.), Vol. 8, pp. 161–227. Academic Press, New York (1972).
7. S. Ostrach and R. G. Hantman, Natural convection inside a horizontal cylinder, *Chem. Engng Commun.* **9,** 213–243 (1981).
8. S. Ostrach, Laminar flows with body forces, in *Theory of Laminar Flows* (edited by F. K. Moore), Vol. 4. High Speed Aerodynamics and Jet Propulsion, Princeton University Press, Princeton, New Jersey (1964).
9. S. Ostrach, Low-gravity fluid flows, *Annual Review of Fluid Mechanics,* Vol. 14 (1982).
10. B. E. Boyack and D. W. Kearny, Heat transfer by laminar natural convection for low aspect ratio cavities, ASME Paper No. 72-HT-52 (1972).
11. S. Ostrach, Natural convection heat transfer in cavities and cells, *Proc. Int. Heat Transfer Conf.,* pp. 365–379. Hemisphere, Washington, DC (1982).
12. B. E. Launder and D. B. Spalding, The numerical computation of turbulent flows, *Comp. Methods Appl. Mech. Engng* **3,** 269 (1974).
13. N. C. Markatos, Transient flow and heat transfer of liquid sodium coolant in the outlet plenum of fast nuclear reactors, *Int. J. Heat Mass Transfer* **21,** 1565 (1978).
14. W. Rodi, Turbulent models and their application in hydraulics—a state of the art review, SFB 80/T/127, University of Karlsruhe (1978).
15. N. C. Markatos, M. R. Malin and G. Cox, Mathematical modelling of buoyancy induced smoke flow in enclosures, *Int. J. Heat Mass Transfer* **25,** 63–75 (1982).
16. D. B. Spalding, A general purpose computer program for multi-dimensional one- and two-phase flow, in *Mathematics and Computers in Simulation,* Vol. XXIII, pp. 267–276. North Holland, Amsterdam (1981).
17. D. B. Spalding, Mathematical modelling of fluid-mechanics, heat-transfer and chemical-reaction processes, A Lecture Course, CFDU Report, HTS/80/1, Imperial College, London (1980).
18. N. C. Markatos, P. J. Phelps and B. Purslow, Computer simulation of the thermal-hydraulic behaviour of fast-reactor pools, *Ann. Nucl. Energy* **9,** 179–193 (1982).
19. S. V. Patankar and D. B. Spalding, A calculation procedure for heat, mass and momentum transfer in three-dimensional parabolic flows, *Int. J. Heat Mass Transfer* **15,** 1787 (1972).
20. I. P. Jones and C. P. Thompson, Numerical solutions for a comparison problem on natural convection in an enclosed cavity, Report No. AERE-R 9955, UKAEA Harwell (1981).
21. G. D. Mallinson and K. A. Pericleous, GRAFFIC: the graphical representation and analysis of fluid flow by interactive computation, CHAM Technical Report, TR/71, June (1981).
22. G. D. Mallinson and G. de Vahl Davis, Three-dimensional natural convection in a box: a numerical study, *J. Fluid Mech.* **83,** 1–31 (1977).
23. M. Jacob, *Heat Transfer,* Vol. 1. Wiley, New York (1949).
24. M. S. Hossain and W. Rodi, Influence of buoyancy on the turbulence intensities in horizontal and vertical jets, in *Heat Transfer and Turbulent Buoyant Convection* (edited by D. B. Spalding and N. Afgan), Vol. 2, pp. 39–51. Hemisphere, Washington, DC (1976).
25. J. W. Elder, Turbulent free convection in a vertical slot, *J. Fluid Mech.* **23,** 99–111 (1965).
26. G. H. Cowan, P. C. Lovegrove and G. L. Quarini,

Turbulent natural convection heat transfer in vertical single water-filled cavities, *Proc. 7th Int. Heat Transfer Conf.*, Vol. 2, pp. 195–201 (1982).
27. W. K. George and S. P. Capp, A theory for natural convection turbulent boundary layers next to heated vertical surfaces, *Int. J. Heat Mass Transfer* **22,** 813–826 (1979).
28. R. K. MacGregor and A. F. Emery, Free convection through vertical plane layers—moderate and high Prandtl number fluids, *Am. Soc. Mech. Engrs*, Series C, *J. Heat Transfer* **91,** 391–403 (1969).
29. A. S. Monin and A. M. Obukov, Basic laws of turbulent mixing in the ground layer of the atmosphere, *Trudy. Geofiz. Inst. An-SSR* **151**(24), 163–187 (1954).

APPENDIX

THE WALL BOUNDARY CONDITIONS

The treatment of wall boundary conditions for turbulent buoyant flows presents a source of uncertainty in the present work. It is therefore worthwhile describing briefly what was done. 'Wall functions' were used for both the laminar and turbulent calculations. In the laminar cases this simply meant that the wall shear stress was evaluated from the presumption of a linear velocity variation between the calculated near-wall value and the zero wall value.

The shear stress calculated in this way was then included as a source term for the velocity component parallel to the wall. For the turbulent calculations, the Reynolds number for the near-wall point was first evaluated. If this was less than 132.25 ($y^+ = 11.5$, the value at which the laminar and turbulent wall-functions intersect) the above laminar wall-function was also used. If the Reynolds number was greater than 132.25, the presumed velocity variation was logarithmic, and the corresponding shear-stress coefficient was evaluated. Both k and ε were fixed at the near-wall grid nodes at the values which would prevail there if indeed the universal logarithmic velocity profile prevailed. The wall heat transfer rate was evaluated from the Chilton–Colburn form of the Reynolds analogy, in which the Stanton number (St) is related to the friction coefficient (C_f) as follows:

$$St = C_f\, Pr^{-2/3}, \tag{A1}$$

where C_f is related to the wall shear stress (τ_w) and the parallel-to-wall velocity $|w|$ as follows:

$$C_f = \tau_w/(\rho\,|w|^2). \tag{A2}$$

The heat transfer rate per unit area at the wall ($\dot{q}''_w$) is then deduced from:

$$\dot{q}''_w = St\,\rho|w|\,C_p(T_p - T_w), \tag{A3}$$

where T_p is the temperature at the grid node in question, and T_w the temperature at the wall.

It is realized that the wall functions may be influenced considerably by temperature variations, and indeed that the logarithmic form used is probably not appropriate since buoyancy effects are ignored in the log layer. A better wall function could be based on either the Monin–Obukov log-linear profile [29], or on the cube root profiles of George and Capp [27].

CONVECTION LAMINAIRE ET TURBULENTE DANS UNE CAVITE FERMEE

Résumé—On présente une méthode numérique pour obtenir des solutions d'écoulement naturel et de transfert de chaleur dans une cavité carrée avec des parois latérales chauffées différemment. On étudie un domaine de nombres de Rayleigh entre 10^3 et 10^6. On utilise une différenciation de cellules donatrices et des études de maillage sont développées pour tous les nombres de Rayleigh considérés. Le modèle de turbulence utilisé pour les nombres de Rayleigh supérieurs à 10^6 est un modèle (k–ε) à deux équations qui inclut les interactions gravité-gradient de masse volumique. Les résultats sont présentés sous forme de tables et de graphiques et de formules de nombres de Nusselt et de Rayleigh. En outre, les résultats de nombres de Rayleigh jusqu'à 10^6 sont comparés avec la solution numérique de Vahl Davis.

LAMINARE UND TURBULENTE FREIE KONVEKTION IN EINEM GESCHLOSSENEN HOHLRAUM

Zusammenfassung—Es wird eine Berechnungsmethode beschrieben, die dazu dient, Lösungen für die laminare und turbulente, von Auftriebskräften bestimmte Strömung und den Wärmeübergang in einem Hohlraum mit quadratischem Querschnitt und unterschiedlich beheizten Seitenwänden zu erhalten. Die Rayleigh-Zahl wurde im Bereich von 10^3 bis 10^6 variiert. Es werden "donor-cell"-Differenzen verwendet. Einflüsse der Gitterverfeinerung wurden bei allen betrachteten Rayleigh-Zahlen untersucht. Als Turbulenzmodell für Rayleigh-Zahlen größer 10^6 wurde ein ($k \sim \varepsilon$)-Modell verwendet, welches Wechselwirkungen zwischen Schwerkraft und Dichtegradienten berücksichtigt. Die Ergebnisse werden in tabellarischer und grafischer Form und als Korrelationen von Nusselt- und Rayleigh-Zahlen dargestellt. Die Ergebnisse für Rayleigh-Zahlen bis 10^6 werden mit den Referenz-Lösungen von de Vahl Davis verglichen.

ЛАМИНАРНАЯ И ТУРБУЛЕНТНАЯ ЕСТЕСТВЕННАЯ КОНВЕКЦИЯ В ЗАМКНУТОЙ ПОЛОСТИ

Аннотация—Описывается численный метод решения задач свободноконвективного ламинарного и турбулентного течения и теплопереноса в квадратной полости с боковыми стенками, нагретыми до разной температуры. Исследования проводились в диапазоне значений числа Релея от 10^3 до 10^{16}. При построении разностной схемы использованы донорские ячейки. Для всех рассматриваемых значений числа Релея проводились исследования влияния измельчения сетки на решение. При значениях числа Релея, превышающих 10^6, использовалась двухпараметрическая ($k \sim \varepsilon$) модель турбулентности, учитывающая взаимодействие между силой тяжести и градиентом плотности. Результаты представлены в виде таблиц и графиков, а также в виде обобщенных зависимостей между числами Нуссельта и Релея. Кроме того, проведено сравнение результатов, полученных при числах Релея, меньших 10^6, с численным решением де Вааль Дависа.